Author's Accepted Manuscript

A Framework Combining Window Width-level Adjustment and Gaussian Filter-based Multi-resolution for Automatic Whole Heart Segmentation

Ken Cai, Rongqian Yang, Huazhou Chen, Lihua Li, Jing Zhou, Shanxing Ou, Feng Liu

Cite this article as: Ken Cai, Rongqian Yang, Huazhou Chen, Lihua Li, Jing Zhou, Shanxing Ou and Feng Liu, A Framework Combining Window Width-level Adjustment and Gaussian Filter-based Multi-resolution for Automatic Whole Heart Segmentation, *Neurocomputing*, http://dx.doi.org/10.1016/j.neucom.2016.03.106

A Framework Combining Window Width-level Adjustment and Gaussian Filter-based Multi-resolution for Automatic Whole Heart Segmentation

Ken Cai[1], Rongqian Yang[2*], Huazhou Chen[3], Lihua Li[2], Jing Zhou[2], Shanxing Ou[4], Feng Liu[5]

[1]School of Information Science and Technology, Zhongkai University of Agriculture and Engineering, Guangzhou, 510225, China

[2]Department of Biomedical Engineering, South China University of Technology, Guangzhou, 510006, China

[3]College of Science, Guilin University of Technology, Guilin, 541004, China

[4]Department of Radiology, General Hospital of Guangzhou Military Command of PLA, Guangzhou, 510010, China

[5]School of Information Technology and Electrical Engineering, the University of Queensland, Brisbane, QLD 4072, Australia

[*]bmeyrq@gmail.com

Abstract

Heart diseases are prevalent among the general population. These diseases can be diagnosed in their early stages through a quantitative evaluation of cardiac functions. In a typical procedure, heart segmentation is initially performed. Quantitative information is then obtained from a 3D reconstructed image of the heart. However, manual segmentation is time-consuming and prone to inter- and intra-observer variations. As such, automatic methods must be developed to assess cardiac functions quantitatively. In this study, an automatic algorithm for whole heart segmentation was established through window width-level adjustment and Gaussian filter-based multi-resolution methods. The proposed algorithm preprocesses the image by adjusting the window width and the centre to acquire cardiac images with clear anatomical structures. The cardiac image is then decomposed into several resolution layers by using a Gaussian filter to eliminate discontinuity associated with traditional pyramid down-sampling and decomposition. A registration-based segmentation algorithm is applied to the cardiac image. The proposed segmentation algorithm was validated with a clinical dataset of 14 cardiac dual-source computed tomography images. Results show that the proposed methods improve the registration accuracy of the epicardium and the endocardium. The volume of the manual segmentation standard is not significantly different from that of the proposed segmentation and the accuracy of the method reaches almost 1 mm in most areas. Thus, the proposed method can be used to perform a high-precision segmentation of the whole heart.

I. INTRODUCTION

The rates of mortality and morbidity associated with cardiovascular diseases have increased over the recent years; these diseases are regarded as the primary cause of death in many countries including China. Patients with heart diseases do not present evident symptoms in their early stages, but suffer from sudden cardiac death after the onset of heart diseases [1]. Therefore, the early quantitative diagnosis and risk assessment of heart diseases is crucial for preventing sudden death and the improving the quality of life of patients.

Computed tomography (CT), magnetic resonance imaging and other imaging technologies are clinically applied to perform cardiac imaging[2-4]. In this process, the cardiac function is analyzed and evaluated based of the heart structure through cardiac image segmentation. Cardiac images are segmented with manual methods that yield precise results, but involve poorly reproducible and time-consuming steps. Manual segmentation requires a significant amount of time, approximately 30 min, to completely process a 3D image that consists of 100–200 2D CT images. Moreover, manual segmentation cannot process a large amount of imaging data to diagnose a heart disease quantitatively. These limitations of manual segmentation have prompted researchers to develop semi-automatic or fully-automatic segmentation methods for cardiac image analysis. However, the development of segmentation techniques remains challenging, because the heart is surrounded by other complex-structured organs.

II. RELATED WORKS

Studies on cardiac chamber segmentation have focused on the left ventricle and have used a model-based segmentation algorithm. This algorithm is usually based on the snake algorithm proposed by Kass [5] and the level set algorithm developed by Sethian [6]; these algorithms are collectively known as active contour models (ACM) and have been widely used in left ventricle segmentation [7-10]. The snake algorithm requires minimal interaction, but exhibits high sensitivity to initial contour, image noise and pseudo boundary. With an appropriate initial contour, it can produce good segmentation results. To avoid the limitations of the traditional snake algorithm, researchers developed a gradient vector flow (GVF) snake algorithm [11, 12] that displays a narrow selective scope of the initial contour. Image deformation relies on the gradient information of images; as such, this algorithm cannot resolve image noise sensitivity and pseudo-boundary problems. The GVF algorithm is also prone to the effects of local gradient information; as a result, the energy function decreases to a local minimum value and yields erroneous segmentation outcomes. The level set algorithm exhibits a higher capacity to overcome noise than does the snake algorithm. The level set algorithm is also used by many researchers to segment 3D and 4D images of the left ventricle [13-15], but this technique presents a narrow selective scope of the initial contour. This algorithm is also difficult to use for developing appropriate conditions for iterative termination.

To overcome the limitations of ACMs and to improve the robustness of their associated algorithms, Shen et al. [16, 17] proposed an active volume model (AVM). The AVM exhibits a higher accuracy in segmenting the left ventricle than do the ACMs. In the initial stage, however, the AVM should be located in the mostly- or completely-segmented region; otherwise, the model might be trapped to the local minimum value and provide inaccurate results. The statistical shape model (SSM) is another technique used to segment the left ventricle [18]. The SSM can be classified into static models (SMs) and generic dynamic models (GDMs). The active shape model (ASM) is a

typical representative of SMs [19-21]. The ASM considers the image morphology, but neglects the changes in space/time dynamics in different time series. However, these models are inappropriate for dynamic image segmentation. For example, GDMs only consider dynamic changes in space and time and disregard alterations in the image morphology. As such, Zhu et al. [22] combined the ASM and GDM to segment the left ventricle of a 4D image of the heart and achieved satisfactory results. In addition to model-based algorithms, the graph cut is a widely-applied technique for segmenting the left ventricle [23-26]. Chen et al. [27] used this method to segment the left ventricle in low-dose CT images and reported satisfactory results. Although the graph-cut algorithm yields good segmentation effects, it is a relatively complex and time-consuming process.

Studies on cardiac chamber segmentation have mainly focused on the left ventricle, although the simultaneous segmentation of the four chambers of the heart is necessary to diagnose lesions in each chamber. Few studies have reported the whole heart segmentation by using the graph-cut algorithm, model-based segmentation algorithms and registration-based segmentation algorithms. Lombaert et al. [28] combined the graph-cut algorithm with motion cubes for a 4D heart segmentation. Nevertheless, this method fails to segment the whole heart, because it considers the four chambers as a whole unit rather than as individual parts. Ecabert et al. [29-31] performed whole heart segmentation through an adaptive geometric model. By contrast, Zheng et al. [32, 33] used a model-based method to segment a 4D image of the whole heart. In these methods, one chamber can only be segmented at a time; consequently, different chambers may overlap one another. Zhuang et al. [34] automatically segmented a 3D image of the whole heart by using a registration-based algorithm in accordance with the average atlas. However, in this algorithm, a standard template should be selected and templates should be matched [35].

In Figure 1, the heart chambers of two individuals with highly similar cardiac DSCT images are characterized by similar location and shape. If the registration algorithm is accurate, single atlas can be used to achieve highly precise cardiac CT image segmentation. This study describes a registration algorithm for the precise registration of cardiac DSCT images in the following sections. The proposed registration algorithm is applied to segment cardiac DSCT images and to achieve high-precise whole heart segmentation.
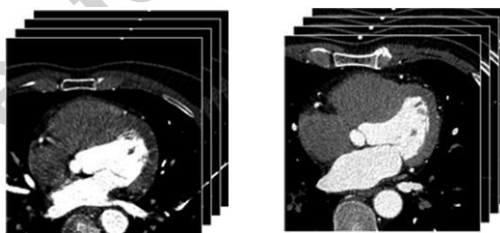

Figure 1. Cardiac DSCT images of two individuals

III. METHODOLOGY

In general, the morphological characteristics of the CT images of the heart from different individuals may be alike, therefore, registration-based segmentation algorithm can be used for whole heart segmentation. This algorithm searches the mapping point of each pixel in the images to be segmented on the template; that is, the template image is registered to the image to be segmented. The parameters of this relationship are recorded during registration and are used to mark and transmit a cardiac atlas with the prior knowledge of medical experts to complete heart segmentation.

Registration accuracy directly affects the accuracy of the segmentation; as such, only a precise registration can accurately complete the whole heart segmentation.

A. Segmentation Framework

A multi-resolution-based method is used to register the template and cardiac DSCT images to be segmented, with the former being the floating image and the latter being the reference image. Figure 2 shows the registration algorithm framework used in this study. For registration-based whole heart segmentation, the cardiac template image is first selected and then labeled. The template selected as the floating image is assigned to the image to be segmented. The transformation parameters of the pixel points from the image to be segmented are mapped to the templates and recorded upon completion of the registration. The atlas with prior knowledge and marked points is transmitted according to the transformation parameter to complete the whole heart segmentation. An appropriate window width level is usually used to preprocess cardiac DSCT images and select those with clear anatomical structures for the registration system. The preprocessed image is used to determine the anatomical structures and pathological characteristics of tissues and organs. After image preprocessing, a Gaussian filter is used to decompose the image into several resolution layers. This process can overcome the discontinuous boundary in traditional pyramid decompositions. To quickly locate the heart in the images, the system adopts a global affine transformation for rough registration. B-spline transformation is also used for the non-rigid deformation of the local heart to achieve precise registration. The mapping points of the pixels of the reference on the floating images do not fall necessarily on the integer pixel positions; thus, an interpolation method is used to calculate the gray values of the points. The interpolation method adopted in this paper is the cubic B-spline interpolation. To control the step length of parameters in the transformation on an adaptive basis, we use the adaptive stochastic gradient descent (ASGD) method proposed by Klein [36] for parameter optimization. Mutual information is used for similarity measurements.
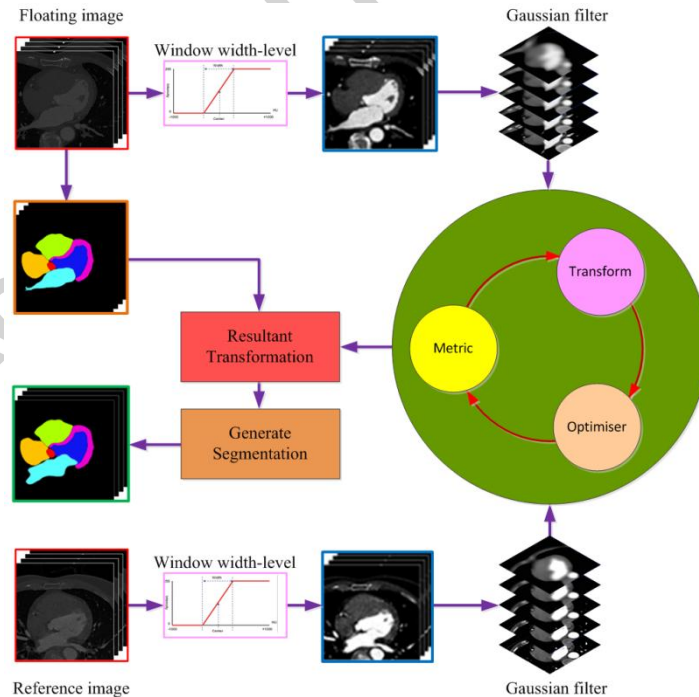

Figure 2. Registration system framework

B. Generation of cardiac atlas label image

The generation of the cardiac atlas label image requires a high-resolution template image to be applicable in all cases. The morphological changes to the heart during the diastolic period are slower than that during the systolic stage. The CT imaging quality is also better in the diastolic stage; thus, the diastolic cardiac DSCT image, with $512 \times 512 \times 170$ pixels, is selected as the template. After template selection, manual segmentation is performed to segment the whole heart from the template. Based on the atrioventricular structure of the heart, we segment the heart into six parts: the aorta (AO), left ventricle (LV), left ventricle myocardium (LVM), left atrium (LA), right ventricle (RV), and right atrium (RA). We manually extract every atrioventricular structure from each 2D CT image. After manual segmentation, we specifically mark each chamber to label the images. Figure 3 illustrates the rendering of the graph, in which the labeled image presents a meticulous structure and reflects the anatomy of the heart.
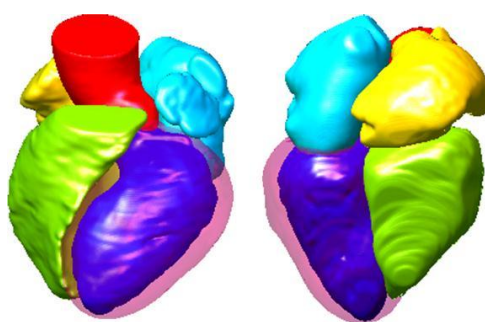

Figure 3. Cardiac atlas label image

C. Window width–level adjustment

Window width and level are two important regulatory factors for acquiring clear medical images. Clinicians tend to adjust the values of these parameters to the most beneficial position for diagnosis. The values are then recorded to provide the information of the Dicom image. Depending on window width/level value, the cardiac DSCT image is adjusted on the gray value. The CT value is converted into the gray value of 0–255, which can clearly display the anatomic structure of the heart. Figure 4 shows the schematic diagram of the images preprocessed with the window width/level method. In the figure, the red curve represents the gray value that corresponds to each CT value after the gray-scale adjustment.
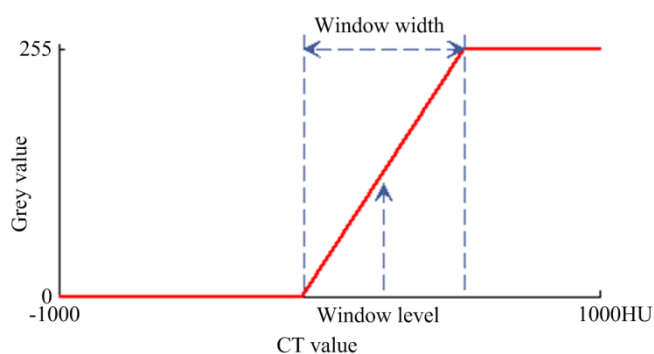

Figure 4. Schematic diagram of window width/level adjustment

Assuming the CT value of a pixel in the image as f(i), window width as ww, and window level as wl, then the value of the pixel point g(i) after preprocessing with window width–level is:

$$g(i) = \begin{cases} 0 & f(i) < wl - 0.5ww \\ \dfrac{f(i) - (wl - 0.5ww)}{\delta} - 1 & wl - 0.5ww \leq f(i) \leq wl + 0.5ww \\ 255 & f(i) > wl + 0.5ww \end{cases} \quad (1)$$

where

$$\delta = ww / 2 5 \qquad (2)$$

The proposed preprocessing method uses the window width/level value adjusted by clinical doctors to modify the pixel values of the cardiac DSCT image. The CT value with an original scope of -1000 HU to 1000 HU is also adjusted to gray levels of 0–255 to reduce image information for easy registration. This method uses the prior knowledge of clinical doctors to reduce image information and enhance contrast in the following: (1) across the contrast agent/myocardium interface for the left heart chambers, (2) between the un-contrasted blood and myocardium in the right chambers and, (3) across the myocardium and outside the heart. Figure 5 shows the preprocessing rendering adjusted with window width/level. The boundary of the pericardium and myocardium exhibits a low contrast before the adjustment, whereas the pericardium is basically filtered after the adjustment; this technique results in clear visualization of the myocardial contour.
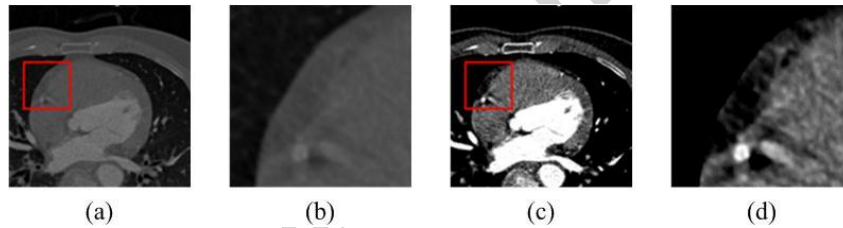

(a)   (b)   (c)   (d)

Figure 5. Rendering of preprocessing with window width–level, (a) before adjustment, (b) local amplification without preprocessing, (c) after adjustment and, (d) local amplification with preprocessing

D. Gaussian filter-based multi-resolution decomposition

The image is decomposed into several resolution layers to improve the convergence speed and precision of the registration algorithm. The low-resolution layer contains the global information of the image. The initial registration of this layer can provide preliminary registration parameters that are used to improve the convergence speed and precision of the high-resolution layers. The traditional pyramid decomposition algorithm uses the down-sampling method to reduce image information layer by layer. However, this method causes a discontinuous boundary of the anatomical structure on the low-resolution layer. To overcome the limitation of the pyramid algorithm, this paper uses the Gaussian filter-based multi-resolution decomposition method in which the filtered image becomes smooth and fuzzy. This characteristic is used to reduce the information of the low-resolution layer. The Gaussian filter works through the image convolution and Gaussian kernel, which should be discretized to filter the digital image. As shown in Figure 6, a discrete Gaussian

kernel function with a width of 20 is used to approach the continuous Gaussian kernel function G(x) that should satisfy the following condition:

$$\int_{x=-\infty}^{\infty} G(x)dx = 1 \qquad (3)$$

Figure 6 shows that the weighted value of the discrete Gaussian kernel function is not equal to 1. Therefore, the discretization process contains an approximation error.
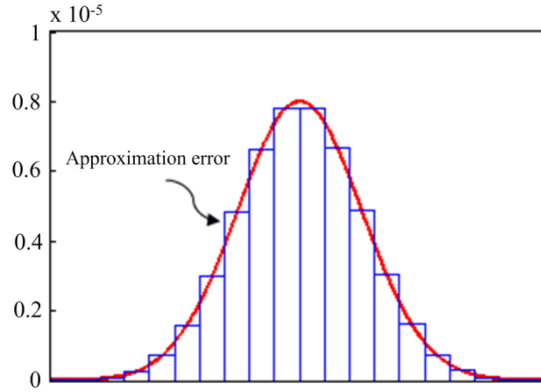

Figure 6. Discretization of Gaussian kernel

The discrete Gaussian kernel function T(n; σ) is reconstructed using the Lindeberg method [37]:

$$T(n;\sigma) = e^{-\sigma^2} I_n(\sigma) \qquad (4)$$

where σ is the variance of the Gaussian kernel function, and $I_n(\sigma)$ is the Bessel function [38]:

$$I_n(\sigma) = \frac{e^{\sigma^2}}{\sqrt{2\pi\sigma}}\left[1 - \frac{4n^2-1}{8\sigma^2} + \frac{(4n^2-1)(4n^2-9)}{2!(8\sigma^2)^2} - \frac{(4n^2-1)(4n^2-9)(4n^2-25)}{3!(8\sigma^2)^3} + \cdots\right] \quad (5)$$

Assuming the allowable approximation error of the Gaussian kernel function as err, then the width of the kernel function l should satisfy the following condition:

$$\sum_{n=1}^{l} T(n;\sigma) = 1 - err \qquad (6)$$

Equations (4) to (6) indicate that under- determined errors; the large variance σ results in the wide kernel function l. At high 1 values, the discrete Gaussian kernel function becomes continuous. Figure 7 shows the 2D Gaussian kernel function with a kernel width of 200×200. The function graph is smooth and the discrete kernel function approximates the continuous function.
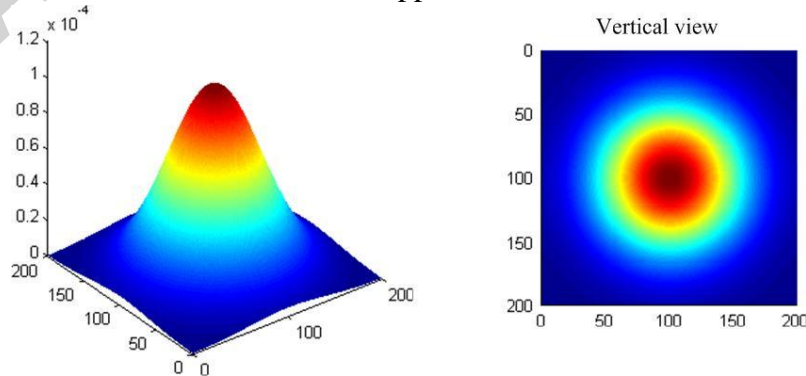

Figure 7. 2D discrete Gaussian kernel function

The experimental results show that the large kernel width l exerts evident effects on the Gaussian filter, resulting in the production of a smoother image. Under a certain approximation error err, l increases with increasing σ. Thus, in this paper, a high σ is set in the low-resolution layer for filtering with a high fuzzy degree to reduce image information, whereas σ is set according to the following formula:

$$\sigma = \frac{\sqrt{2^{L-level}}}{s} \tag{7}$$

where L is the total number of resolution layers; level is the current resolution layer, whose minimum value is in the first layer; and s is the space between two adjacent pixels.

Figure 8 shows the images decomposed by the multi-resolution method. Furthermore, Figure 8(a) illustrates the checkerboard phenomenon in the low-resolution images that are decomposed using the pyramid algorithm. This phenomenon decreases the accuracy of the registration. Figure 8(b) also shows the multi-resolution images obtained by the Gaussian filter-based multi-resolution decomposition. The low-resolution image is fuzzy and the obtained information is reduced; nevertheless, the images still show continuous boundaries.
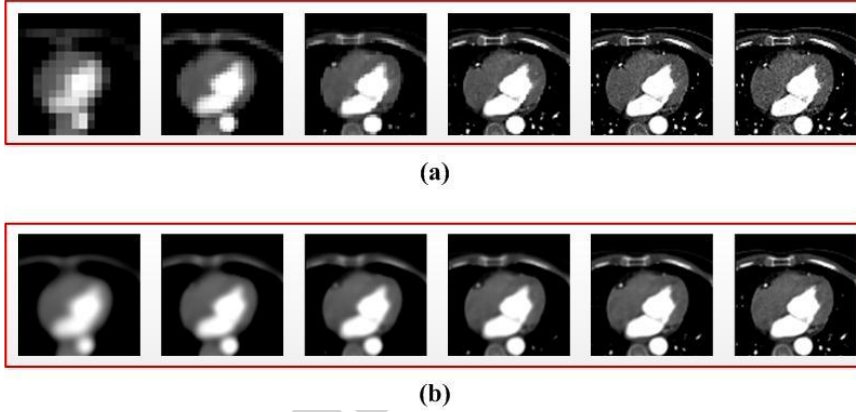

(a)

(b)

Figure 8. Multi-resolution decomposition. (a) pyramid decomposition and (b) Gaussian filter-based multi-resolution decomposition

E. Global affine transformation and free-form deformations

The central location and long axis direction of the heart differ among the cardiac images of different individuals. To quickly locate the heart, we use the affine transformation for global transformation of the cardiac image to analyze a rough registration. B-spline transformation is then used for the local and non-rigid transformation of the heart to improve the local accuracy of the registration.

Affine transformation is used to achieve the translation, scaling and rotational transformation of the images. This technique employs a simple mathematical operation for a matrix and an addition product, resulting in fast computation. Thus, this paper uses affine transformation to determine the initial position of the heart [39].

Assuming the coordinates of a pixel in the reference image as x, then the mapping point on the floating image can be represented as:

$$\boldsymbol{T_{\mu}(x) = A(x) + t} \tag{8}$$

where t is the translation matrix, and A is the rotation, shear and scaling matrix. The parameters of the affine transformation are given by $\mu = [a, t_x]^T$. Initial parameters should be set before the transformation. This paper considers the differences in the floating and reference image centres as the initial value of the translational matrix by moving the centre of the floating image to overlap to the centre of the reference image. If the centre of the floating images is x_{mc} and the centre of the reference image is x_{fc}, the initial translation matrix t is:

$$t = x_{mc} - x_{fc} \tag{9}$$

The initial value of a is the direction cosine matrix of the coordinate system of the two images. The unit vectors of the three axes of the reference image are x_1, x_2, and x_3. The unit vectors of the three axes of the floating image are e_1, e_2, and e_3, respectively, where $x_1 = x_f$, $x_2 = y_f$, $x_3 = z_f$, $e_1 = x_m$, $e_2 = y_m$, and $e_3 = z_m$. The direction cosine b_{ij} between e_i and x_j is:

$$b_{ij} = \cos(\theta_{ij}) = e_i \cdot x_j \tag{10}$$

The direction cosine matrix B is:

$$B = \begin{bmatrix} b_{11} & b_{12} & b_{13} \\ b_{21} & b_{22} & b_{23} \\ b_{31} & b_{32} & b_{33} \end{bmatrix} \tag{11}$$

Both reference and floating images are obtained through DSCT sampling. Thus, the coordinate systems of the two images are similar, and the direction cosine matrix is:

$$B = \begin{bmatrix} x_f x_m & x_f y_m & x_f z_m \\ y_f x_m & y_f y_m & y_f z_m \\ z_f x_m & z_f y_m & z_f z_m \end{bmatrix} = \begin{bmatrix} 1 & 0 & 0 \\ 0 & 1 & 0 \\ 0 & 0 & 1 \end{bmatrix} \tag{12}$$

Therefore, the initial parameter of the affine transformation μ_0 is $(1, 0, 0, 0, 1, 0, 0, 0, 1, x_{mc}-x_{fc}, y_{mc}-y_{fc}, z_{mc}-z_{fc})^T$.

To improve the accuracy of the registration, we use a B-spline transformation after the affine transformation [39]. The B-spline transformation uses a set of grid points to control image deformation. Assuming the $n_x \times n_y \times n_z$ mesh of the control points covering the reference images as Φ_x, then the spacing of these points in three directions are presented as δ. The mapping point of point x can be represented as:

$$T_\mu(x) = x + \sum_{x_k \in \Phi_x} \phi_k \beta^3(\frac{x - x_k}{\delta}) \tag{13}$$

where x_k is the control point, ϕ_k is the B-spline coefficient vectors, and $\beta^3(x)$ is the cubic multidimensional B-spline polynomial.

All the coordinates of the grid points in Φ_x are regarded as the parameter μ of the B-spline transformation. This paper adopts the following strategies for parameter initialization to set the space of grid points in each direction:

$$\delta = \delta_0 \times 2^{L-level} \times \frac{newlength}{oldlength} \tag{14}$$

where L is the total number of the resolution layer, level is the current resolution layer, oldlength is the original width of the reference images in this direction, newlength is the mapping width of the reference image after the affine transformation, and δ_0 (5 mm) is the initial grid space set through clinical experience. This strategy generates few grid points in the low-resolution layer and dense grids in the high-resolution layer, thereby increasing the registration speed in the low-resolution layer and the registration accuracy in the high-resolution layer.

After the grid spacing is determined, the initial parameters of the B-spline transformation in the first layer are set as the coordinate values of the grid points. The subsequent solution layers use the transform parameter result μ_{l-1} of the previous layer as the initial parameter μ_l. The number of points of μ_l is higher than that of μ_{l-1}; thus, we interpolate between the points of the previous layer grid to obtain the missing points of the high-resolution grid.

In digital imaging, only integer points have the corresponding gray values. Points on the reference images can be mapped to the non-integer points to search for the mapping relationship. To assign mapping points, we use the surrounding pixels for interpolation. Cubic B-spline interpolation is also used to calculate the gray value of the mapping point. Interpolation is then performed based on the pixels of the small $4 \times 4 \times 4$ (Ω_x) area surrounding the mapping point. The pixel coordinates of the mapping point are set as x, where x_k is the pixel coordinates of the integer points in the small area. The gray values of the mapping point after the cubic B-spline interpolation are given by:

$$f(\boldsymbol{x}) = \sum_{\boldsymbol{x}_k \in \Omega_x} \boldsymbol{c}_k \beta^3 (\boldsymbol{x} - \boldsymbol{x}_k) \tag{15}$$

where c_k is the coefficient of the B-spline interpolation and can be calculated by recursive filtering.

F. Mutual information-based registration cost function

This paper uses the Parzen window-based mutual information to measure the registration degree [40]. Mutual information is a physical quantity representing the overlapping degree of two images. A high coincidence results in a large mutual information. Registration is used to achieve the maximum mutual information and the minimum cost function through parameter optimization. The adaptive gradient descent [36] proposed by Klein is used for parameter optimization and negative information is used as the cost function:

$$C(\boldsymbol{\mu}) = -MI = -\sum_{\iota \in L_M} \sum_{\kappa \in L_F} p(\iota, \kappa; \boldsymbol{\mu}) \log_2 \left(\frac{p(\iota, \kappa; \boldsymbol{\mu})}{p_F(\kappa) p_M(\iota; \boldsymbol{\mu})} \right) \tag{16}$$

The joint histograms of the reference and floating images are divided into several segments, where LM and LF are the number of segments, ι and κ are the histogram indices, and $p(\iota, \kappa; \mu)$ is the joint probability distribution of the reference and floating images estimated using the Parzen Window [41]:

$$p(\iota, \kappa; \boldsymbol{\mu}) = \frac{1}{|\Omega_F|} \sum_{\boldsymbol{x}_i \in \Omega_F} \beta^0 \left(\kappa - \frac{f_F(\boldsymbol{x}_i) - f_F^{\circ}}{\Delta b_F} \right) \cdot \beta^3 \left(\iota - \frac{f_M(\boldsymbol{T}(\boldsymbol{x}_i; \boldsymbol{\mu})) - f_M^{\circ}}{\Delta b_M} \right) \tag{17}$$

where Ω_F is the sample point set used to estimate the joint probability; $|\Omega_F|$ is the number of sample points; f_F and f_M are the values of the reference and floating images, respectively; f_F° and f_M° are the minimum values of the images; Δb_F and Δb_M are the widths of each segment in the joint histogram;

β^0 and β^3 are the zero order and the cubic B-spline function, respectively; and $p_F(\kappa)$ and $p_M(\iota; \mu)$ are the marginal probabilities of the reference and floating images, respectively.

$$p_F(\kappa) = \sum_{\iota \in L_M} p(\iota, \kappa; \boldsymbol{\mu}) \tag{18}$$

$$p_M(\iota; \boldsymbol{\mu}) = \sum_{\kappa \in L_F} p(\iota, \kappa; \boldsymbol{\mu}) \tag{19}$$

IV. RESULTS AND VALIDATION

A. Dataset acquisition and elaboration

In this section, we employed 15 volunteer data sets acquired on the DSCT scanning system (Definition Somatom 2008G) equipped with Syngo 8.0 Multi Modality and Aquarius iNtuition Architecture at the General Hospital of Guangzhou Military Command in PLA. Prior to scanning, the contrast agent iopromide (370 mgI/ml) was injected. The injection rate for the adults was 3.5–6 ml/s, and the total dose was 60–90 ml; whereas, the injection rate for the teenagers was 1.2–3.0 ml/s, and the total dose was 20–85 ml. After injecting iopromide, all the people scanned were injected with 44 ml of NS at a rate of 5 ml/s. During scanning, the patient must maintain a resting state and those who could not cooperate were given chloral hydrate to pacify them. The parameters of the scanner were set as follows: tube voltage, 120 KV; tube current, 380–400 mA; machine tool rotation time, 0.33 s; collimation width, 64 mm × 0.6 mm (cardiac mode); and screw pitch, 0.2–0.43 mm under automatic modulated according to the heart rate. After scanning with retrospective ECG gating, the original material was reconstructed to obtain 21 time phases between 0–100% at 5% R-R interphase, with a reconstruction spacing of 1 mm. In the acquired images, a 3D diastolic cardiac image with 512 × 512 × 170 pixel size was selected as the floating image and registered to two random cases acquired at the cardiac diastolic and systolic periods. In the experiments, the images should be initially preprocessed through window width/level adjustment. The floating and reference images were then decomposed into six resolution layers. In the Gaussian filtering multi-resolution decomposition, the approximation error of the discrete Gaussian kernel function err was set as 0.01, and the initial grid space of the B-spline transformation was 5 mm. For parameter iteration optimization, the gradient descent optimization of the registration by the affine transformation and B-spline deformation on each layer took 500 and 1000 iterations, respectively.
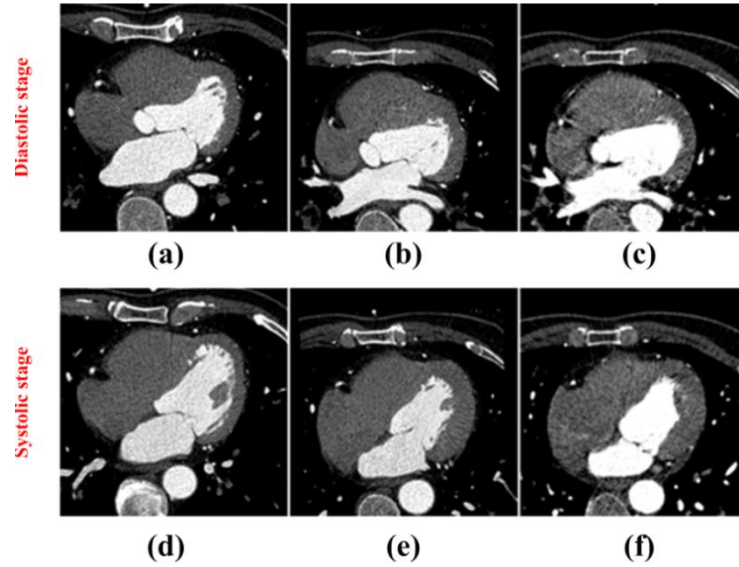
Figure 9. Cardiac DSCT image registration, (a) floating image, (b) registration results, (c) reference image in the diastolic stage, (d) floating image, (e) registration results and, (f) reference image in the systolic stage

Figure 9 shows two registration cases, where (a)–(c) are the registration results of the reference image in the diastolic stage, and (d)–(f) are the registration results of the reference image in the systolic stage. For convenience, the selected CT images were compared at the same positions of the heart. The registration results of the two experiments are accurate and the floating and reference images exhibit minimal differences after the registration.

The proposed method was experimentally evaluated to compare and analyze the registration accuracy of the Gaussian filter-based multi-resolution decomposition and the window width/level-based preprocessing method (SW). The following techniques were used for the experiment: Gaussian filter-based multi-resolution decomposition without a window width/level-based preprocessing method (SNW), pyramid down-sampling multi-resolution decomposition with a window width/level-based preprocessing method (RW), and a pyramid down-sampling multi-resolution decomposition without a window width/level-based preprocessing method (RNW). During the multi-resolution decomposition, the images were decomposed into six resolution layers by using the two decomposition methods. Table 1 records the mutual information before and after the registration. Mutual information between the reference and floating images was minimal before the registration, regardless of whether the reference image was in the systolic or diastolic stage. By contrast, the mutual information increased to different degrees after the registration. The Gaussian filter-based multi-resolution decomposition method evidently increased the mutual information compared with the pyramid down-sampling multi-resolution decomposition method, thereby significantly improving the optimization process leading to a more efficient registration.

Table 1. Mutual information of each method before and after the registration

Cardiac status of reference images	Before registration	SW	SNW	RW	RNW
Diastolic period	0.241362	1.695359	1.614266	1.018358	1.106956
Systolic stage	0.237128	1.618931	1.622510	1.000664	1.184208

Figures 10 and 11 show the changes in the mutual information value after each iteration. The first 3000 iterations represent the affine iterative transformation of the six resolution layers, whereas the final 6000 iterations denote the B-spline iterative transformation process. The mutual information of each method in the affine transformation decreased with the increasing resolution layer; this finding could be caused by two factors: image information increases as the resolution layer increases and affine transformation captures only the global motion of the heart. Using the pyramid down-sampling method to decompose images in the B-spline transformation, we found that the mutual information decreased with the increasing resolution layer, as shown in Row 2 of Figures 10 and 11. The Gaussian filter method can improve the mutual information value layer by layer, as shown in Row 1 of Figures 10 and 11. Therefore, Gaussian filter-based multi-resolution decomposition may exert better effects than the pyramid down-sampling decomposition.
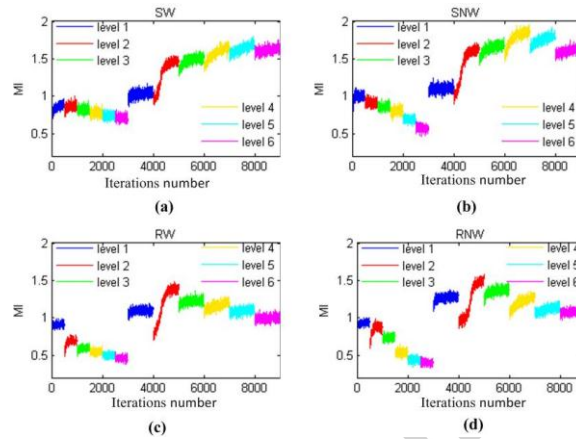

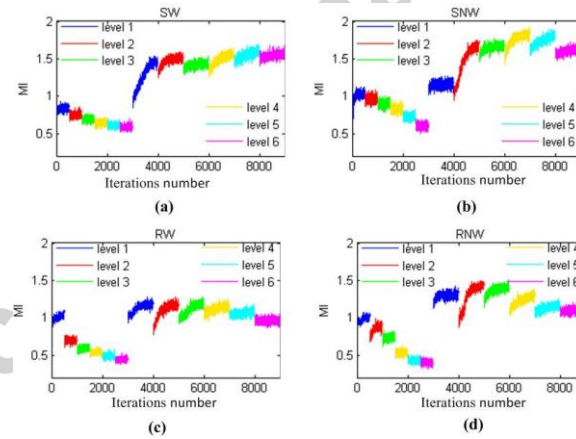Figure 10. Distribution of mutual information value with the number of iterations in the diastolic stage

Figure 11. Distribution of mutual information value with the number of iterations in the systolic stage

Table 1 and Figures 10 and 11 show that preprocessing with window width/level adjustments did not significantly improve the mutual information under the same multi-resolution decomposition conditions. However, this method can improve the registration accuracy of the epicardium. Columns 1 and 2 in Figures 12 and 13 represent the fusion images of the floating and reference images after the registration, respectively, whereas Columns 3 and 4 denote the local magnification corresponding to the boundary colour. The fusion method is the alternate superposition of the two images masked by a checkered pattern. As indicated by the red arrow, an evident dislocation appears beyond the

epicardium of the registration without window width/level adjustment. The floating and reference images are consistent in the registration after the preprocessing.
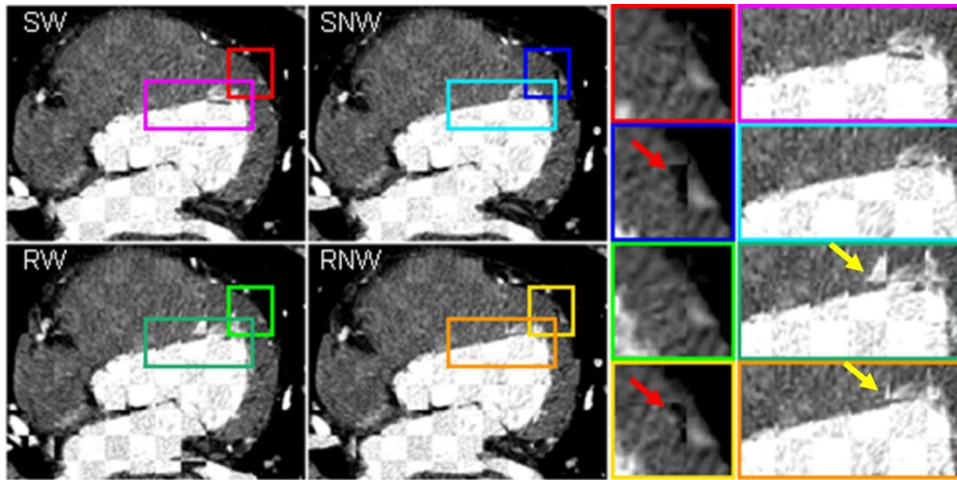

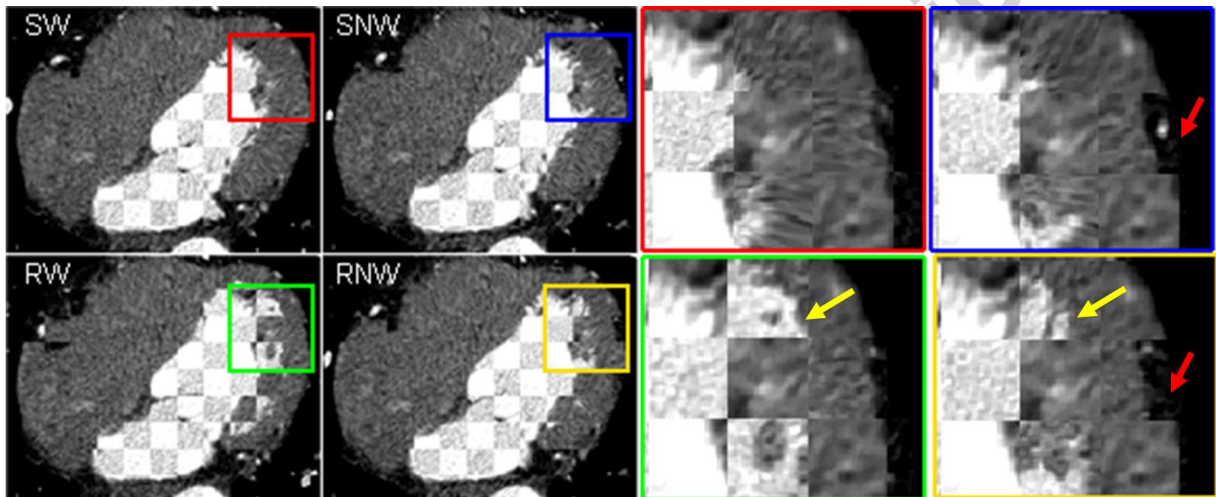Figure 12. Fusion of floating and diastolic reference images after the registration

Figure 13. Fusion of floating and systolic reference images after the registration

The yellow arrow indicates the myocardial dislocation in the down-sampling decomposition method. The Gaussian filter-based multi-resolution decomposition method proposed in this paper obtained satisfactory results with good fitness. Thus, the proposed method can improve the registration accuracy of the myocardium.

B. Registration and segmentation analyses

The whole heart DSCT 3D segmentation algorithm was implemented based on the registration with SW. The algorithm was applied to a dataset of 14 cardiac DSCT images that were acquired in the cardiac diastolic stage. The size of the CT image was 512×512 pixels and the image layer was between 117 and 265. Figure 14 shows the comparison of the results from the proposed and manual segmentation methods in different layers. The segmentation contour line obtained from the fully-automatic segmentation algorithm is similar to that from the manual segmentation method. In addition, the proposed algorithm exhibited good segmentation effects with a clear heart structure and a complete atrioventricular structure. Tissues beyond the heart, such as the rib and the diaphragm,

were precisely segmented. Thus, this method can accurately segment a 3D image of the whole heart from cardiac DSCT images.
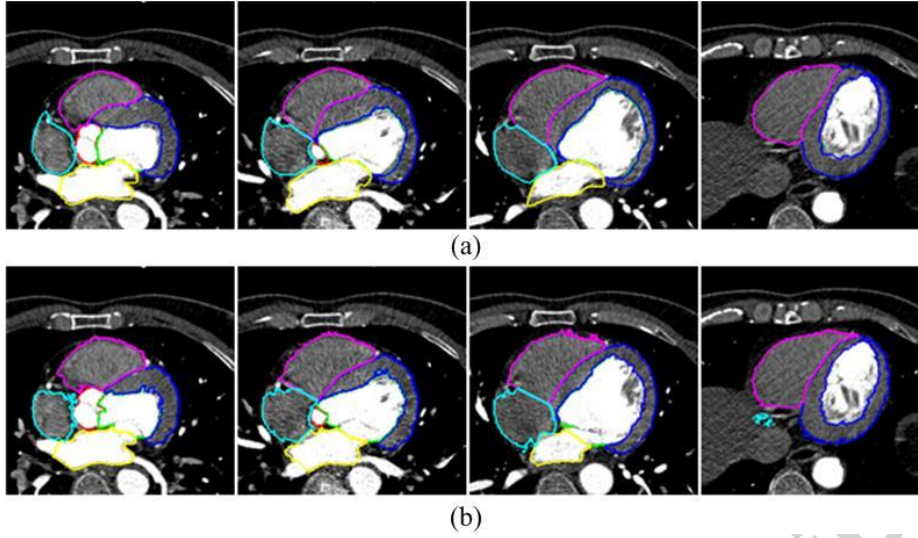

Figure 14. Comparison between (a) manual segmentation and (b) proposed method

This paper compared the proposed automatic segmentation method with manual segmentation as the gold standard and analyzed the precision of both techniques. Manual segmentation was performed by a clinician with knowledge of the heart anatomy and double-checked by cardiologists. Two methods were used for the statistical analysis of segmentation accuracy from the 14 datasets; these methods included volume measurement-based similarity analysis and surface distance measurement-based error analysis. The similarity degree between automatic segmentation and manual segmentation results can be calculated through volume overlap and dice coefficients. As the two values become closer to 1, the automatic segmentation results approximate the manual segmentation results. The calculation methods of these two parameters are shown in the following formulae:

$$\text{VolumeOverlap} = \frac{\left|V_{\text{seg}} \bigcap V_{\text{gd}}\right|}{\left|V_{\text{seg}} \bigcup V_{\text{gd}}\right|} \tag{20}$$

$$\text{DiceCofficient} = \frac{2\left|V_{\text{seg}} \bigcap V_{\text{gd}}\right|}{\left|V_{\text{seg}}\right| + \left|V_{\text{gd}}\right|} \tag{21}$$

where V_{gd} and V_{seg} represent the volume of the gold standard and the automatic segmentation methods, respectively.

Table 2 shows the calculation results of the mean volume overlap and dice coefficients in the test dataset of the 14 cases. A high similarity was observed between the automatic segmentation and manual segmentation results.

Table 2 Measurement error of the whole heart volume

Measuring area	Volume Overlap Coefficient	Dice Coefficient
AO	0.89±0.05	0.94±0.03

LV	0.85±0.04	0.92±0.03
LVM	0.65±0.08	0.78±0.06
LA	0.82±0.06	0.90±0.04
RV	0.65±0.11	0.78±0.09
RA	0.71±0.11	0.82±0.08

Surface distance is the minimum distance between each point on the surface of a manually and automatically-segmented heart. The measurement of this parameter can intuitively evaluate the precision of the automatic segmentation results. At a small distance, the results of the automatic segmentation method become similar to the gold standard. Distance can be calculated as:

$$d_i = \min(\left| \boldsymbol{x}_{\mathrm{gd}i} - \boldsymbol{x}_{\mathrm{seg}} \right|) \tag{22}$$

Figure 15 shows the distribution of the surface-to-surface error of one case. Most segmentation errors are below 1 mm, suggesting the high precision of the automatic segmentation. The segmentation accuracy reaches 5 mm in the minute region, such as junction between RV and LVM and between RV and pulmonary artery. This finding could be caused by the inability of manually distinction between blood and myocardial tissues in the absence of the contrast agent perfusion.
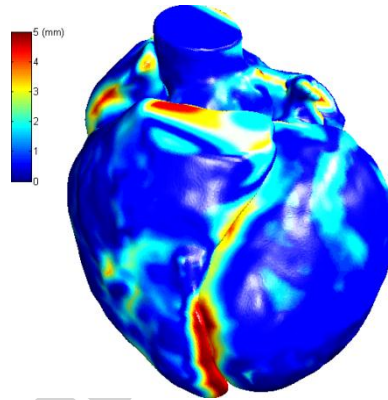

Figure 15. Distribution of surface-to-surface error

Figure 16 shows the Box-and-Whisker chart of the average error from each surface distance in the segmentation of the 14 datasets using the proposed method. The figure reflects the average error distribution of each image. The mean segmentation errors of AO, LV, LVM and LA are highly concentrated, most of which being below 2 mm. This finding proves that the method exhibits satisfactory robustness in the segmentation of these parts. However, some samples present higher average errors in RV and RA, although the segmentation accuracy in most of the samples is about 2 mm. The dispersion of the RA precision in the automatic segmentation algorithm is mainly affected by two factors. First, the right heart segment was not injected with a contrast agent at image acquisition; thus, no obvious boundary between RA and RV was established. The two segments are also difficult to separate even with manual segmentation. Second, the boundary between the right ventricle and pulmonary artery is unclear.
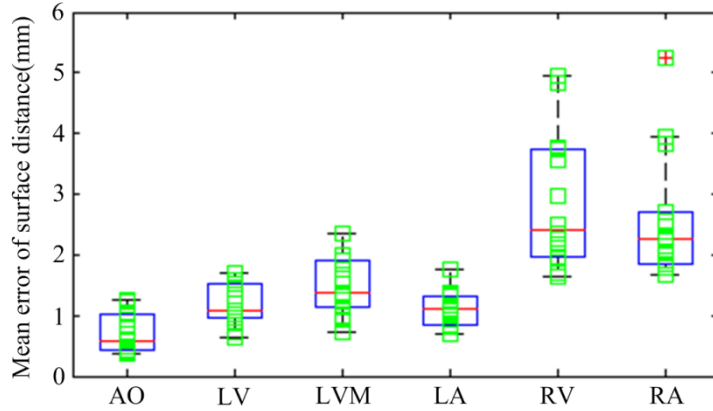
Figure 16. Box-and-Whisker chart of mean surface distance error at each part from 14 cases using the proposed segmentation

To verify the role of the SW registration on improving the accuracy of segmenting the 3D whole heart image, we applied the SW, SNW, RW, and RNW to the test dataset of 14 cases at the same time and analyzed surface distance errors. Figure 17 shows the Box-and- Whisker chart of the surface distance error of the whole heart segmentation when using the four methods. Compared with the other methods, the SW has a relatively concentrated mean error of the whole heart segmentation in each sample image, which is distributed between 1–2.5 mm. The general segmentation error is also lower in the SW than that in the other methods. Thus, the proposed method exhibits higher accuracy and robustness in the 3D whole heart segmentation.
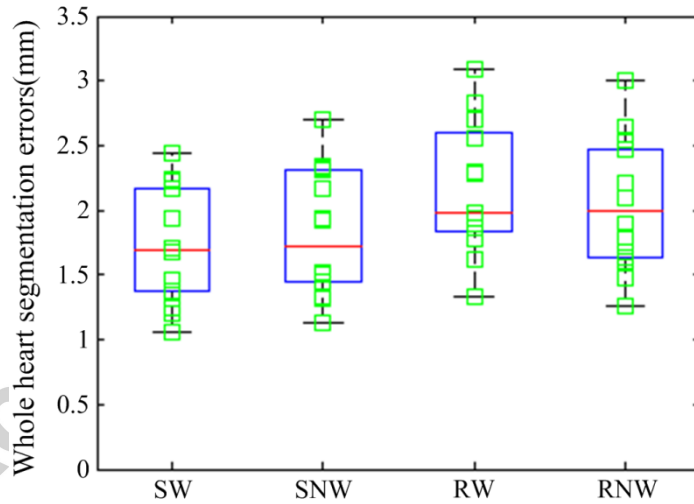

Figure 17. Box-and-Whisker chart of mean surface distance error of the 14 cases using different methods

V. DISCUSSION AND CONCLUSION

The tissue structure in medical images can be clearly displayed through the window width/level adjustment and decomposition of a discontinuous boundary of images via pyramid down-sampling. As such, this study used the window width/level-based method to preprocess the reference and floating images. The Gaussian filter method was then applied to decompose the images into multiple resolution layers for the precise registration with affine transformation and precise registration with

B-spline non-rigid transformation. Our experimental results revealed that the proposed Gaussian filter-based multi-resolution decomposition can overcome the discontinuity problems in the down-sampling decomposition method. Mutual information can be significantly improved during the registration. This method can also improve the accuracy of the registration results in the endocardium. Preprocessing with window width-level adjustments can enhance the registration results in the epicardium. A detailed cardiac atlas is used for the 3D cardiac DSCT image segmentation, and the SW segmentation results were similar to manual segmentation results. These results also exhibited a smooth contour. Considering the precision of the 3D segmentation results, we concluded that the proposed SW registration method provided clear advantages in whole heart segmentation over traditional methods. In particular, the proposed registration-based segmentation method exhibits a higher precision in those major areas than do traditional methods. However, more research is required to develop improved segmentation approaches, that can be used to enhance the accuracy of the segmentation of RA and RV that are not injected with a contrast agent.

Acknowledgement

Reference

[1] W. Hua, L.F. Zhang, Y.F. Wu, X.Q. Liu, D.S. Guo, H.L. Zhou, Z.P. Gou, L.C. Zhao, H.X. Niu, K.P. Chen, J.Z. Mai, L.N. Chu, S. Zhang, Incidence of sudden cardiac death in China: analysis of 4 regional populations, Journal of the American College of Cardiology, 54 (2009) 1110-1118.

[2] J. Maiora, B. Ayerdi, M. Graña, Random forest active learning for AAA thrombus segmentation in computed tomography angiography images, Neurocomputing, 126 (2014) 71-77.

[3] T. Zhang, Y. Xia, D.D. Feng, A clonal selection based approach to statistical brain voxel classification in magnetic resonance images, Neurocomputing, 134 (2014) 122-131.

[4] L. Liu, W. Lin, J. Pan, M. Jin, X-ray computed tomography using sparsity based regularization, Neurocomputing, 173, Part 2 (2016) 256-269.

[5] M. Kass, A. Witkin, D. Terzopoulos, Snakes: Active contour models, International Journal of Computer Vision, 1 321-331.

[6] J.A. Sethian, Level set methods and fast marching methods: evolving interfaces in computational geometry, fluid mechanics, computer vision, and materials science (Cambridge university press, 1999).

[7] L. Spreeuwers, M. Breeuwer, Detection of left ventricular epi-and endocardial borders using coupled active contours, International Congress Series, (Elsevier2003), pp. 1147-1152.

[8] J. Cho, P.J. Benkeser, Cardiac segmentation by a velocity-aided active contour model, Computerized Medical Imaging and Graphics, 30 (2006) 31-41.

[9] H.-Y. Lee, N.C. Codella, M.D. Cham, J.W. Weinsaft, Y. Wang, Automatic left ventricle segmentation using iterative thresholding and an active contour model with adaptation on short-axis cardiac MRI, Biomedical Engineering, IEEE Transactions on, 57 (2010) 905-913.

[10] Y. Zhou, W.-R. Shi, W. Chen, Y.-l. Chen, Y. Li, L.-W. Tan, D.-Q. Chen, Active contours driven by localizing region and edge-based intensity fitting energy with application to segmentation of the left ventricle in cardiac CT images, Neurocomputing, 156 (2015) 199-210.

[11] Y. Chenoune, C. Pellot-Barakat, C. Constantinides, R.E. Berbari, M. Lefort, E. Roullot, E. Mousseaux, F. Frouin, Methodology for Jointly Assessing Myocardial Infarct Extent and Regional Contraction in 3-D CMRI, Biomedical Engineering, IEEE Transactions on, 59 (2012) 2650-2659.

[12] C.-M. Chen, H.H.-S. Lu, Y.-C. Lin, An early vision-based snake model for ultrasound image segmentation, Ultrasound in medicine & biology, 26 (2000) 273-285.

[13] I.-C. Tsai, Y.-L. Huang, K.-H. Kuo, Left ventricular myocardium segmentation on arterial phase of multi-detector row computed tomography, Computerized Medical Imaging and Graphics, 36 (2012) 25-37.

[14] F. Khalifa, G.M. Beache, G.G. Farb, G.A. Giridharan, A. El-Baz, Accurate automatic analysis of cardiac cine images, Biomedical Engineering, IEEE Transactions on, 59 (2012) 445-455.

[15] M. Lynch, O. Ghita, P.F. Whelan, Segmentation of the left ventricle of the heart in 3-D+ t MRI data using an optimized nonrigid temporal model, Medical Imaging, IEEE Transactions on, 27 (2008) 195-203.

[16] T. Shen, H. Li, X. Huang, Active volume models for medical image segmentation, Medical Imaging, IEEE Transactions on, 30 (2011) 774-791.

[17] T. Shen, H. Li, Z. Qian, X. Huang, Active volume models for 3D medical image segmentation, Computer Vision and Pattern Recognition, 2009. CVPR 2009. IEEE Conference on, (IEEE2009), pp. 707-714.

[18] D. Fritz, D. Rinck, R. Dillmann, M. Scheuering, Segmentation of the left and right cardiac ventricle using a combined bi-temporal statistical model, Medical Imaging, (International Society for Optics and Photonics2006), pp. 614121-614121-614110.

[19] S.P. Brien, O. Ghita, P.F. Whelan, A Novel Model-Based 3D Time Left Ventricular Segmentation Technique, Medical Imaging, IEEE Transactions on, 30 (2011) 461-474.

[20] H.C. Van Assen, M.G. Danilouchkine, M.S. Dirksen, J.H. Reiber, B.P. Lelieveldt, A 3-D active shape model driven by fuzzy inference: application to cardiac CT and MR, Information Technology in Biomedicine, IEEE Transactions on, 12 (2008) 595-605.

[21] X. Qin, Y. Tian, P. Yan, Feature competition and partial sparse shape modeling for cardiac image sequences segmentation, Neurocomputing, 149, Part B (2015) 904-913.

[22] Y. Zhu, X. Papademetris, A.J. Sinusas, J.S. Duncan, Segmentation of the left ventricle from cardiac MR images using a subject-specific dynamical model, Medical Imaging, IEEE Transactions on, 29 (2010) 669-687.

[23] A. Eslami, A. Karamalis, A. Katouzian, N. Navab, Segmentation by retrieval with guided random walks: Application to left ventricle segmentation in MRI, Medical image analysis, 17 (2013) 236-253.

[24] J. Ulén, P. Strandmark, F. Kahl, An efficient optimization framework for multi-region segmentation based on lagrangian duality, Medical Imaging, IEEE Transactions on, 32 (2013) 178-188.

[25] I.B. Ayed, H.-m. Chen, K. Punithakumar, I. Ross, S. Li, Max-flow segmentation of the left ventricle by recovering subject-specific distributions via a bound of the Bhattacharyya measure, Medical image analysis, 16 (2012) 87-100.

[26] K. Punithakumar, I. Ben Ayed, A. Islam, I.G. Ross, S. Li, Tracking endocardial motion via multiple model filtering, Biomedical Engineering, IEEE Transactions on, 57 (2010) 2001-2010.

[27] X. Chen, M.S. Nacif, S. Liu, C. Sibley, R.M. Summers, D.A. Bluemke, J. Yao, A framework of whole heart extracellular volume fraction estimation for low-dose cardiac CT images, Information Technology in Biomedicine, IEEE Transactions on, 16 (2012) 842-851.

[28] H. Lombaert, F. Cheriet, Spatio-temporal segmentation of the heart in 4d mri images using graph cuts with motion cues, Biomedical Imaging: From Nano to Macro, 2010 IEEE International Symposium on, (IEEE2010), pp. 492-495.

[29] O. Ecabert, J. Peters, H. Schramm, C. Lorenz, J. Von Berg, M.J. Walker, M. Vembar, M.E. Olszewski, K. Subramanyan, G. Lavi, Automatic model-based segmentation of the heart in CT images, Medical Imaging, IEEE Transactions on, 27 (2008) 1189-1201.

[30] J. Peters, O. Ecabert, C. Meyer, R. Kneser, J. Weese, Optimizing boundary detection via simulated search with applications to multi-modal heart segmentation, Medical image analysis, 14 (2010) 70-84.

[31] O. Ecabert, J. Peters, M.J. Walker, T. Ivanc, C. Lorenz, J. von Berg, J. Lessick, M. Vembar, J. Weese, Segmentation of the heart and great vessels in CT images using a model-based adaptation framework, Medical image analysis, 15 (2011) 863-876.

[32] Y. Zheng, A. Barbu, B. Georgescu, M. Scheuering, D. Comaniciu, Fast automatic heart chamber segmentation from 3D CT data using marginal space learning and steerable features, Computer Vision, 2007. ICCV 2007. IEEE 11th International Conference on, (IEEE2007), pp. 1-8.

[33] X. Zhuang, K.S. Rhode, R.S. Razavi, D.J. Hawkes, S. Ourselin, A registration-based propagation framework for automatic whole heart segmentation of cardiac MRI, Medical Imaging, IEEE Transactions on, 29 (2010) 1612-1625.

[34] M. Cabezas, A. Oliver, X. Lladó, J. Freixenet, M.B. Cuadra, A review of atlas-based segmentation for magnetic resonance brain images, Computer methods and programs in biomedicine, 104 (2011) e158-e177.

[35] D. Mattes, D.R. Haynor, H. Vesselle, T.K. Lewellen, W. Eubank, PET-CT image registration in the chest using free-form deformations, Medical Imaging, IEEE Transactions on, 22 (2003) 120-128.

[36] Jiang D, Ying X, Han Y, et al. Collaborative multi-hop routing in cognitive wireless networks[J]. Wireless Personal Communications, 2015: 1-23.

[37] Lv Z, Tek A, Da Silva F, et al. Game on, science-how video game technology may help biologists tackle visualization challenges[J]. PloS one, 2013, 8(3): 57990.

[38] Yang J, Chen B, Zhou J, et al. A low-power and portable biomedical device for respiratory monitoring with a stable power source[J]. Sensors, 2015, 15(8): 19618-19632.

[39] Y. Zhang, G. Zhou, J. Jin, X. Wang, A. Cichocki. Optimizing spatial patterns with sparse filter bands for motor-imagery based brain-computer interface. Journal of Neuroscience Methods, vol. 255, pp. 85-91, 2015.

[40]Fasheng Wang, Mingyu Lu. Efficient Visual Tracking via Hamiltonian Monte Carlo Markov Chain. Computer Journal. 5 6(9):1102-1112, 2013.

[41] Lin Y, Yang J, Lv Z, et al. A self-assessment stereo capture model applicable to the internet of things[J]. Sensors, 2015, 15(8): 20925-20944.

Biography

Feng Liu received his PhD degree in biomedical engineering in 2000 from Zhejiang University, China. He joined the University of Queensland in 2000. Dr Liu's expertise lies in medical imaging. His primary contribution has been in the areas of (1) MRI hardware design and electromagnetic analysis; (2) cardiac electrical function imaging. He has over 260 publications to date including over 100 fully refereed journal papers and seven patents (three of them have been licensed to the MRI industry). He is also heavily involved in collaborative and consulting projects with industry partners around the world.

Huazhou Chen received the Ph.D degree in applied mathematics from Shanghai University, China, in 2011. He is an Assistant Professor in College of Science, Guilin University of Technology, China. His research interests include computational biology, bio- and chemo- informatics and digitized-spectrum analytical technology.


Jing Zhou is a lecturer and is studying for her doctorate in the Department of Biomedical Engineering, South China University of Technology, Guangzhou, Guangdong, China. Her research interests include medical image processing and biomedical signals detection and processing.

Ken Cai received the B.S. degree in measurement and control technology and instrumentation from Guangdong University of Technology, Guangzhou, China, in 2003, the M.S. degree measurement and control technology and instrumentation from Guangdong University of Technology, Guangzhou, China, in 2006, and the Ph.D. degree in biomedical engineering from South China University of Technology, Guangzhou, China, in 2011. He is an associate professor from the School of Information Science and Technology, Zhongkai University of Agriculture and Engineering, Guangzhou, China. His main research areas include machine vision and biomedical instrument.

Lihua Li received the B.S. degree in biomedical engineering from South China University of Technology, Guangzhou, China, in 2010, the M.S. degree in biomedical engineering from South China University of Technology, Guangzhou, China, in 2013. Her main research areas include image processing and biomedical instrument.
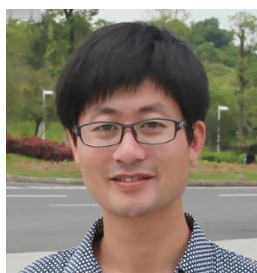
Rongqian Yang received the B.S. degree in electronic instrumentation and measurement from Nanchang Institute of Aeronautical Technology, Nanchang, China, in 2001, the M.S. degree in communication and information systems from Jinan University, Guangzhou, China, in 2005, and the Ph.D. degree in biomedical engineering from Shanghai Jiao Tong University, Shanghai, China, in 2009. He is an associate professor from the Department of Biomedical Engineering, South China University of Technology, Guangzhou, China. His main research areas include machine vision and biomedical instrument.

Shanxing Ou received his masterr degree of the first military medical University at Guangzhou of China in 1996 and his doctor degree of the Second military medical University for imaging diagnosis at shanghai of China in 2004. His current research interests include the cardiac imaging diagnosis, earlier diagnosis of pulmonary cancer as well as liver, and computed aided diagnosis. Now he is the chairman of the department of radiology at general hospital of Guangzhou military command of PLA in china.